Signature of slab fragmentation and dynamic interaction between slabs and the mantle transition zone in northeast Asia

Jung-Hun Song[1], Seongryong Kim[2], and Junkee Rhie[1]

[1]Seoul National University
[2]Korea University

November 24, 2022

Abstract

Slab subduction imaged by seismic tomography implies extensive mantle convection and circulation in the Earth's interior. Widespread subduction of the western Pacific plate beneath the eastern Eurasian plate has left peculiar geochemical and geophysical signatures in the upper mantle of East Asia, which allow to investigate the extent of thermochemical interactions between the subducting plates and the surrounding mantle. Here we provide refined images of the stagnant Pacific slab and the mantle transition zone beneath northeast Asia. We applied teleseismic traveltime tomography and 3-D body-wave waveform modeling by using high-quality datasets from dense seismic arrays including in the Korean Peninsula and southwestern Japan, and found a clear signature of fragmentation of the stagnant Pacific slab. We imaged a localized low-velocity anomaly with high Vp/Vs ratio at 410-km depth above the slab gap, which was interpreted to be partial melting. The segmented Pacific slab reflects a rapid change in boundaries between the Pacific plate, Eurasian plate, and Philippine Sea plate during the Early to mid-Miocene. The slab fragmentation likely has facilitated localized mantle convection in the upper mantle and the mantle transition zone around the slab segments. Our images provide evidence of dynamic interplay between the evolving plate configurations, subducting slabs, and the surrounding mantle.

Signature of slab fragmentation and dynamic interaction between slabs and the mantle transition zone in northeast Asia

DI45D-0048

Jung-Hun Song[1](wjdgns230@snu.ac.kr), Seongryong Kim[2], Junkee Rhie[1]
[1]School of Earth and Environmental Sciences, Seoul National University, Seoul, Korea, [2]Department of Earth and Environmental Sciences, Korea University, Seoul, Korea

Abstract

Subducting slab imaged by seismic tomography indicates extensive mantle convection and circulation in the Earth's interior. Widespread subduction of the western Pacific plate beneath the eastern Eurasian plate has left peculiar geochemical and geophysical signatures in the upper mantle of East Asia, which allows to investigate the extent of thermochemical interactions between the subducting plates and the surrounding mantle. Here we provide refined images of the stagnant Pacific slab and the mantle transition zone beneath northeast Asia. We applied teleseismic traveltime tomography and 3-D body-wave waveform modeling by using high-quality datasets from dense seismic arrays including in the Korean Peninsula and southwestern Japan, and found a clear signature of fragmentation of the stagnant Pacific slab. We imaged a localized low-velocity anomaly with high Vp/Vs ratio at 410-km depth above the slab gap, which was interpreted to be partial melting. The segmented Pacific slab reflects a rapid change in boundaries between the Pacific plate, Eurasian plate, and Philippine Sea plate during the Early to mid-Miocene. The slab fragmentation likely has facilitated localized mantle convection in the upper mantle and the mantle transition zone around the slab segments. Our images provide evidence of dynamic interplay between the evolving plate configurations, subducting slabs, and the surrounding mantle.

Data & Methods

Seismic stations & Events

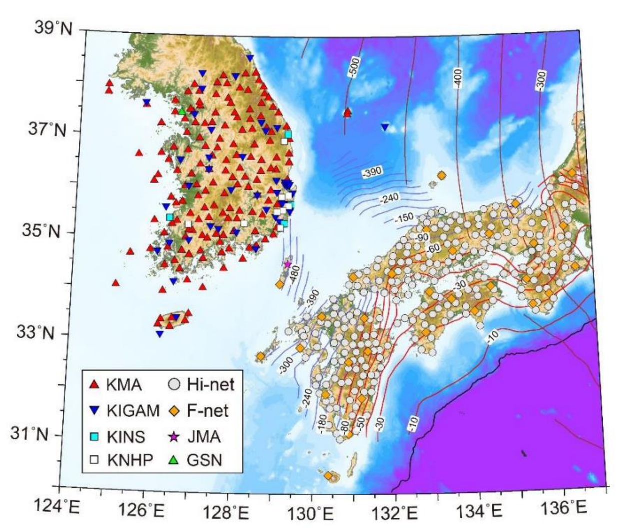

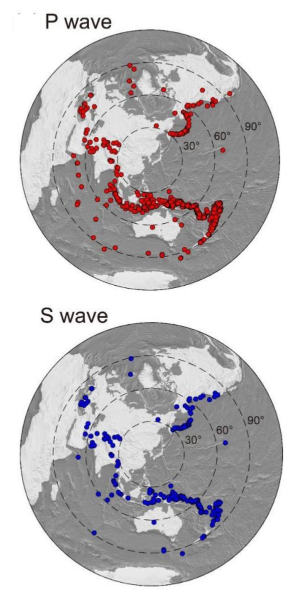

Figure (a) shows seismic stations used in this study. Stations from different networks are shown in different color and symbol. KMA: Korea Meteorological Administration; KIGAM: Korea Institute of Geoscience and Mineral Resources; KINS: Korea Institute of Nuclear Safety; KNHP: Korea Hydro and Nuclear Power; F- and Hi-net: networks of National Research Institute for Earth Science and Disaster Resilience; JMA: Japan Meteorological Agency; GSN: Global Seismic Network. The brown solid contours indicate subducting Pacific slab at 50-km intervals (Hayes et al., 2018). The red and blue contours indicate subducting Philippine Sea slab at 10-km and 30-km intervals, respectively.

Figures (b) shows distribution of teleseismic events used for P and S wave tomography. The dashed black circles are plotted at 30° increments.

Relative traveltime measurement & Data inversion

Relative arrival time residuals were measured by the adaptive stacking method (Rawlinson et al., 2004). We processed *P* and *S* waveforms, respectively, in vertical component filtered in 0.1-5.0 Hz and in transverse component filtered in 0.1-1.0 Hz. We applied Fast Marching Tomography (FMTOMO, Rawlinson & Urvoy, 2006) to invert data residuals to construct 3-D P and S wave velocity models. This method applies the fast marching method (FMM, Rawlinson & Sambridge, 2004), which is a grid-based eikonal solver, for calculating wave propagation in a 3-D local model space, and the subspace inversion technique (Kennett et al., 1988) for data inversion. Forward traveltime calculation and the inversion procedure were iteratively applied to solve a non-linear tomography inversion problem. We simultaneously inverted for the crust and upper mantle structures with initial 3-D crustal structure from CRUST 1.0 (Laske et al., 2013).

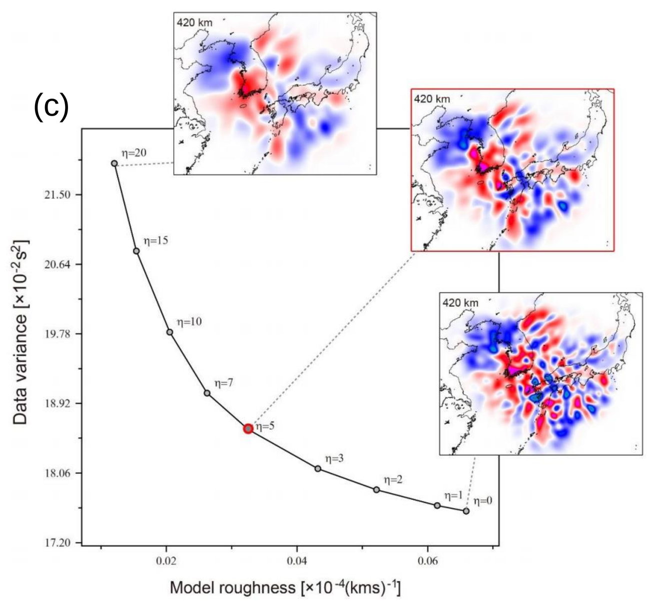

Constructing Vp/Vs model

We performed joint inversion of and wave dataset to construct the 3-D Vp/Vs structure by simultaneously inverting the P and S wave datasets with an additional smoothing regularization on the smoothness of Vp/Vs. To reduce possible artefacts from different ray density of each individual dataset on results, data with common source-receiver pairs are only used, consisting of 86,918 rays for 516 sources. We determined the smoothing parameter for Vp/Vs based on the trade-off between the total data misfit and model smoothness while maintaining regularization factors for individual datasets determined in individual inversions (**Figure c**). We weighted each dataset according to the inverse proportion of the size of each data vector to balance the contribution of different datasets to the overall data. We calculated Vp/Vs variations based on the ak135 reference model, noting that different settings of the 1-D reference model have a minor influence on the resulting perturbation.

Tectonic setting

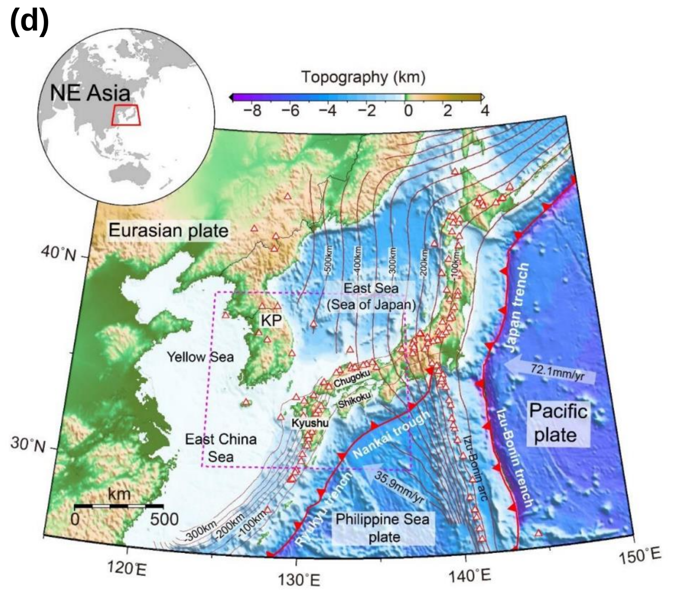

Figure (d) shows regional tectonic map of northeast Asia. Convergent plate boundaries are shown with red saw-toothed lines. Depths of the subducting oceanic slabs are indicated by brown solid (Pacific slab) and dashed (Philippine Sea slab) contours at 50-km intervals based on the Slab2 model (Hayes et al., 2018). Volcanoes are indicated by red triangles. A pink dashed rectangular box shows the map boundary of Figure 3.2. KP: Korean Peninsula.

Tomography Results

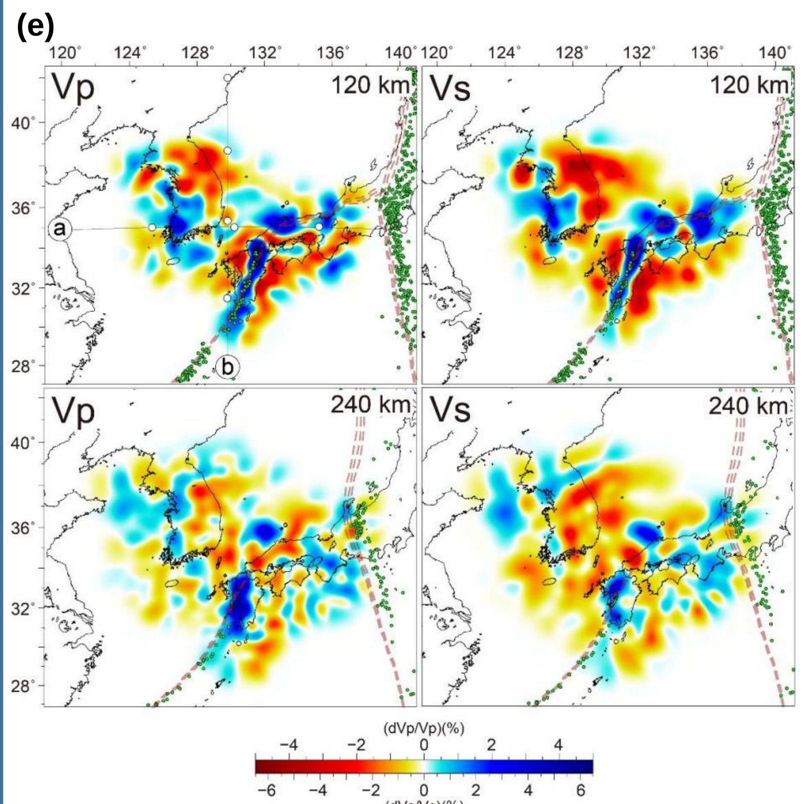

Figure (e) shows horizontal cross-sections through the (Vp; left) and (Vs; right) wave tomography at depths of 120 and 240 km. The green dots indicate earthquakes that occurred within a depth range of ±15 km for the sliced depths. The brown dashed contours indicate slab depths at 10-km intervals within a depth range of ±15 km for the sliced depths.

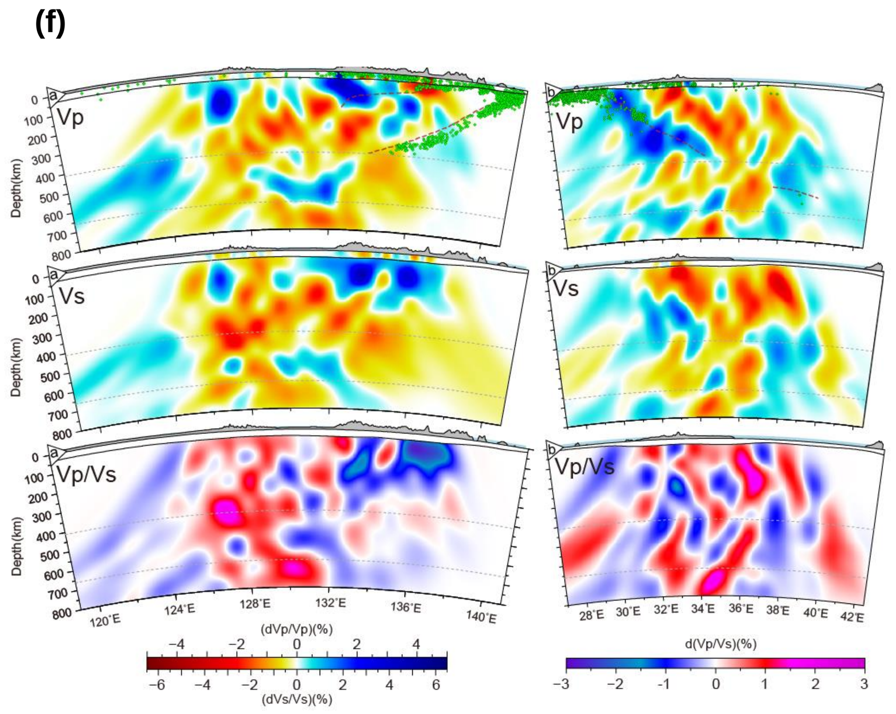

Figure (f) shows vertical cross-sections of (Vp; top) and (Vs; middle) wave tomography, and the Vp/Vs (bottom). The locations of the cross-sections are shown in the 390 km depth profile of Vp in Figure 3.10. Green-dots represent earthquakes within an orthogonal distance range of ±0.5 degree from each cross sections.

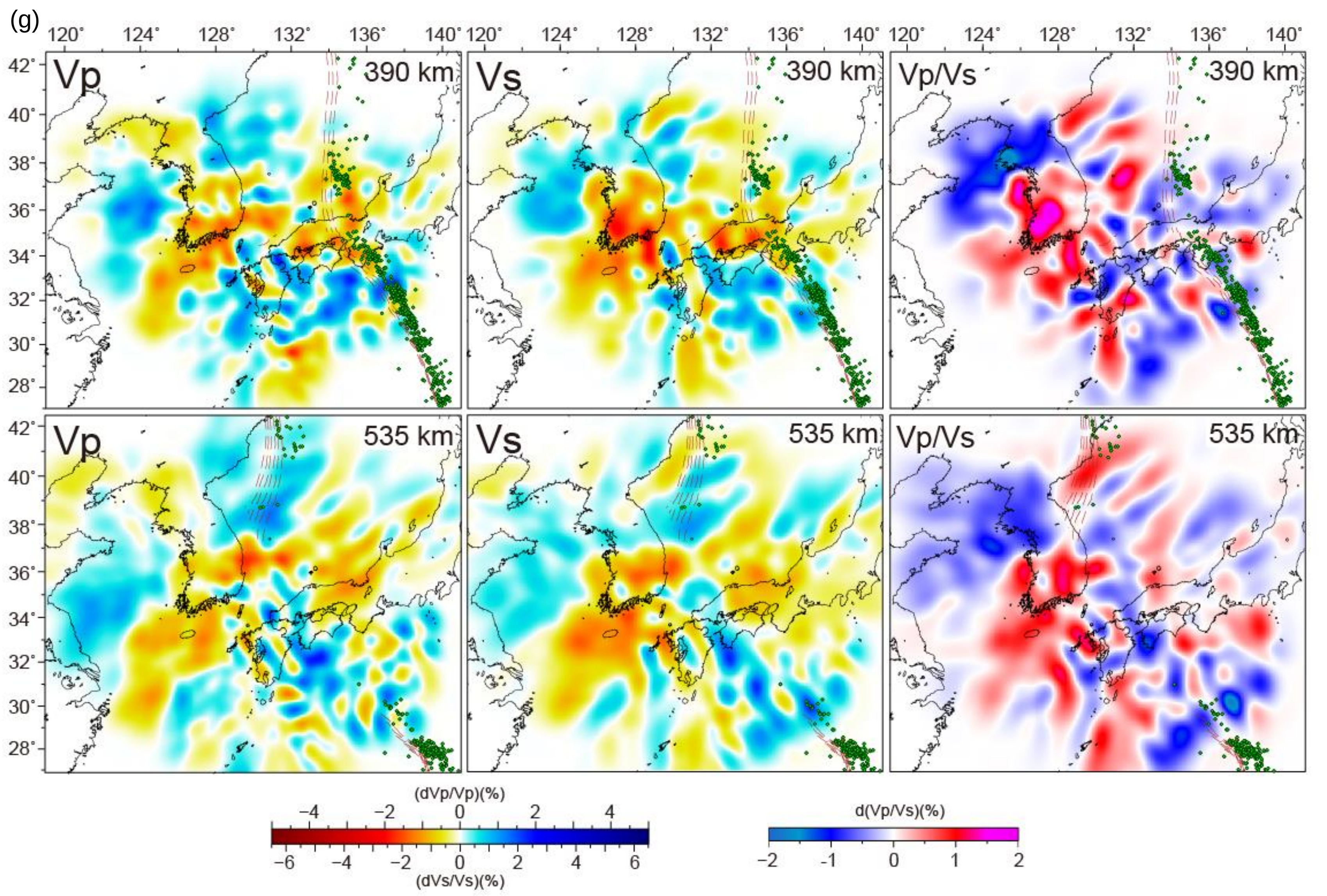

Figure (g) shows horizontal cross-sections through (Vp; left) and (Vs; middle) wave tomography, and the Vp/Vs (right) at depths of 390 and 535 km. Slab depths and earthquakes are indicated by brown dashed contours and green dots, respectively, within a depth range of ±15 for the 390 km and ±30 km for the 535 km depth profiles.

Resolution tests

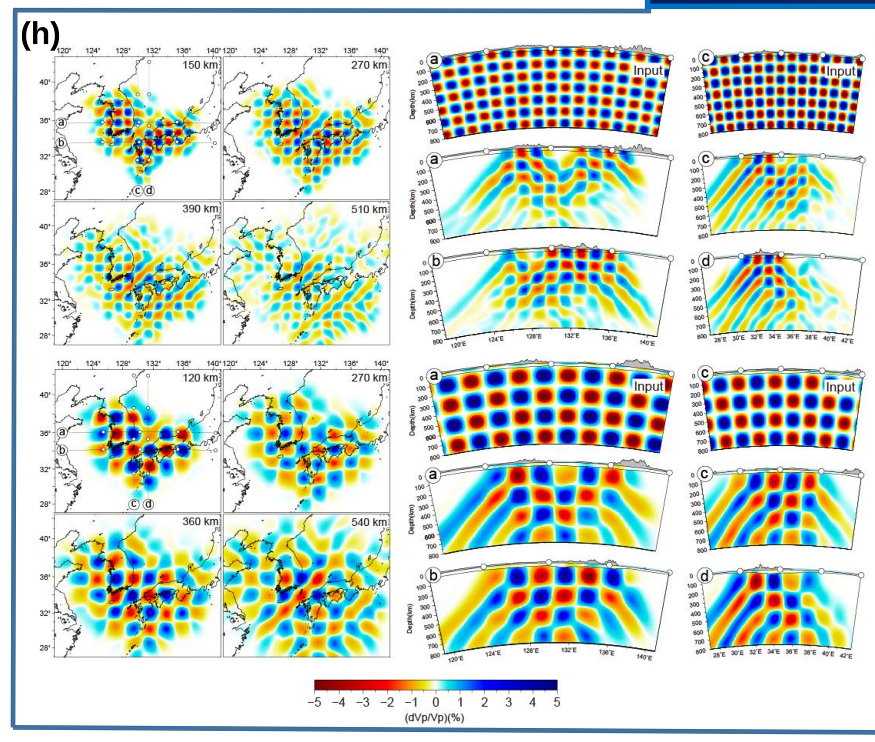

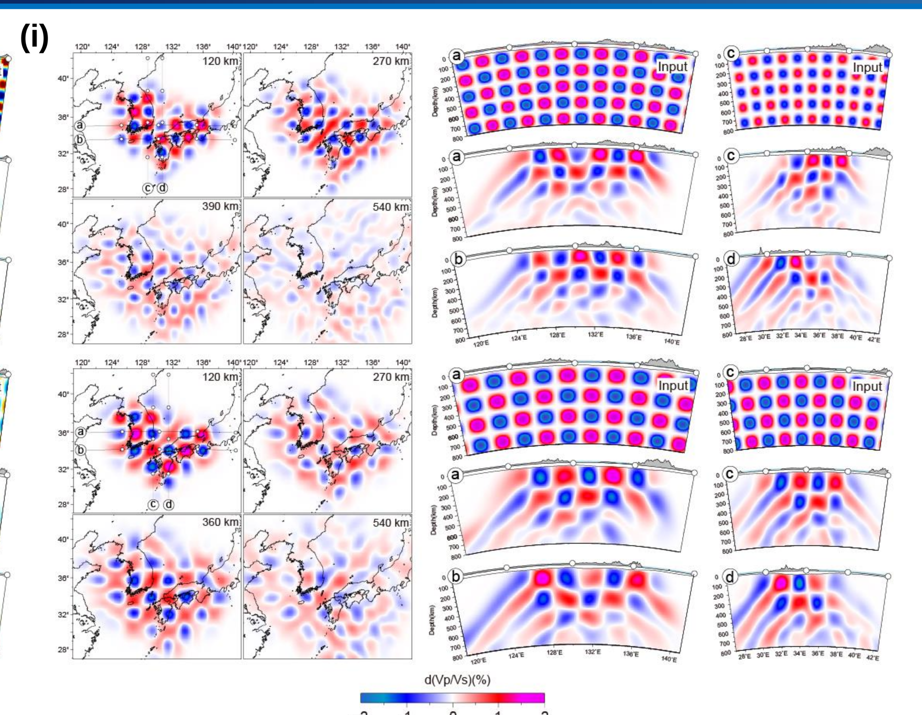

Figure (h) shows checkerboard resolution test results for P wave tomography. Checkers with sizes of 90 and 150 km and amplitudes of ±4% for Vp are shown. **Figure (i)** shows checkerboard resolution test results for the Vp/Vs. Checkers with sizes of 120 and 150 km and amplitudes of ±3% for Vp/Vs are shown. **Figure (j)** shows structural resolution test results of the P wave tomography. (Left) Synthetic model consisting of a plate-like high-velocity anomaly with a size of ~300 km in horizontal and ~80 km in vertical with an amplitude of ~3% of dVp at the bottom of the MTZ. (Right) Synthetic model consisting of the same high-velocity anomaly added with low-velocity layers with a thickness of ~50 km and an amplitude of -5% of dVp right above the MTZ. The inputs and their corresponding outputs are shown in the first and second rows, respectively.

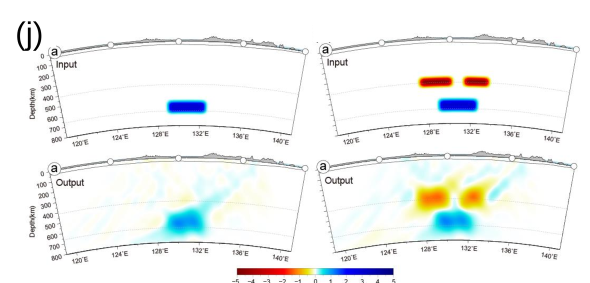

The mantle transition zone heterogeneity

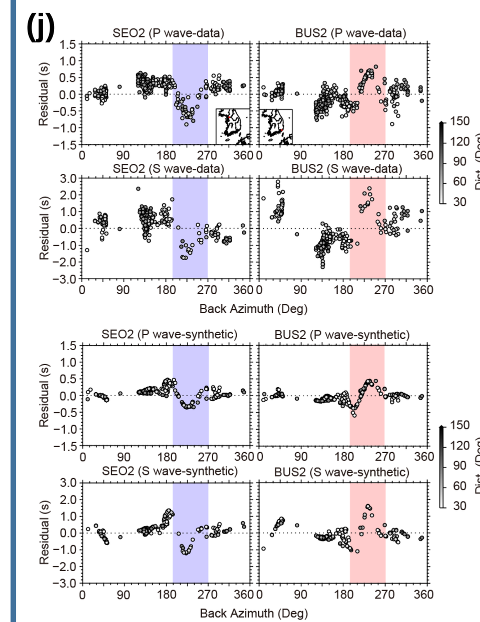

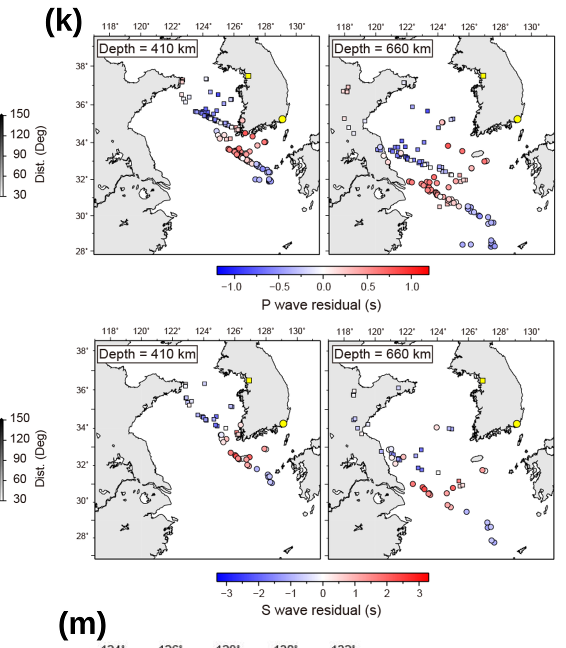

Evidence 1: Residuals

Figure (j) shows back-azimuthal variation in P and S wave travel time residuals and comparison with synthetic residuals. Top panels show the observed residual plots for stations SEO2 (left) and BUS2 (right). The locations of stations are indicated by the red dot in the inset maps. The blue and red shades indicate degree ranges of sharp residual variations. Bottom panels show synthetic residual plots for stations SEO2 (left) and BUS2 (right) using regional 3-D and wave velocity models of Tao et al., 2018 at depths from 400 to 800 km.

Figure (k) shows P and S wave residuals of the two stations projected onto the 410 (left) and 660 (right) km. The yellow squares indicate station locations.

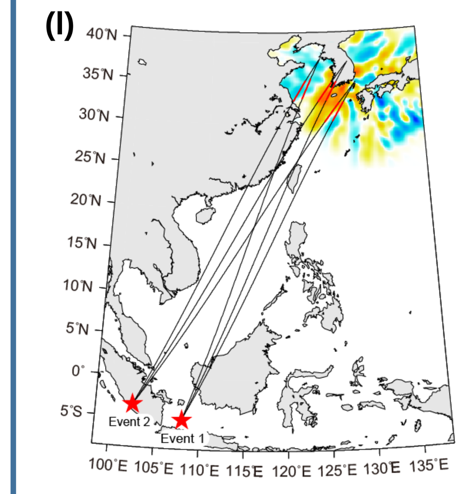

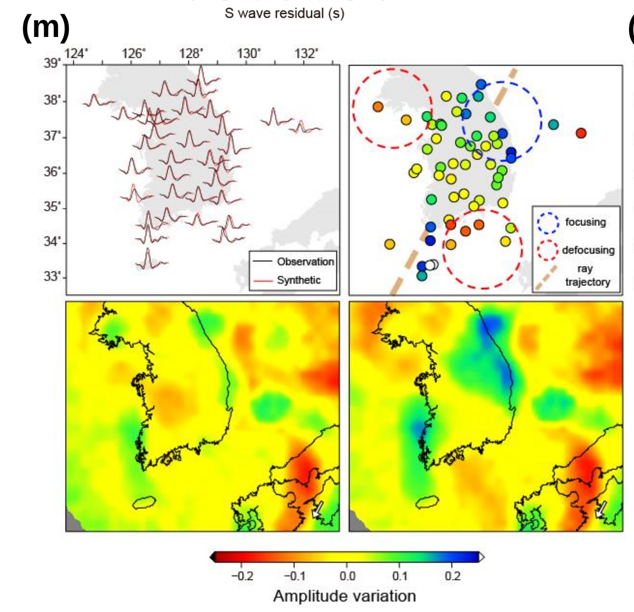

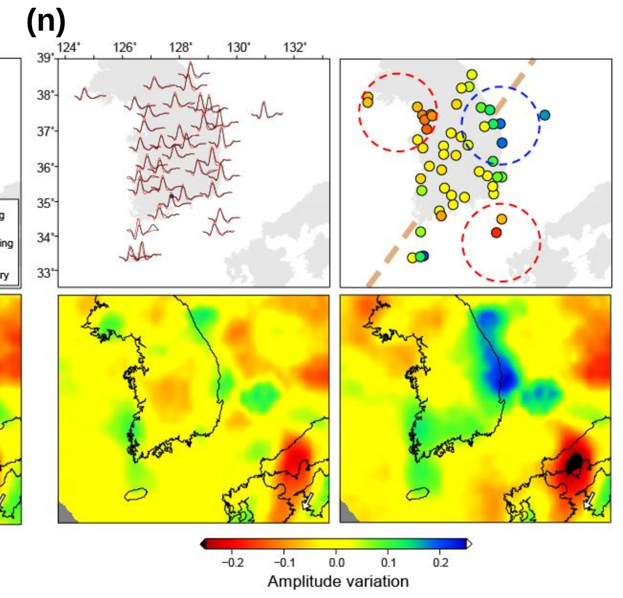

Evidence 2: Waveforms

Figure (l) shows the events, ray trajectories, and the velocity model (Vs at a depth of ~560 km) used for waveform simulations (Komatitsch & Tromp, 1999). Black solid lines represent the ray trajectories from the events with parts of rays crossing the depth between 660 and 410 km on the receiver side indicated by the red lines.
Figure (m) (Top-left) Comparison of observed (black) and synthetic (red) transverse component waves for Event 1. (Top-right) Amplitude variation of the observed waveform. The amplitude variation is calculated as the difference between the amplitude of the waveform at each receiver and the average amplitude of all receivers on a logarithmic scale. The area where the wave amplitude is amplified (reduced) by wave focusing (defocusing) is indicated by blue (red) dashed circle. (Bottom-left) Synthetic amplitude variation with a 3-D model using only the upper mantle at depths less than 350 km. (Bottom-right) Synthetic amplitude variation with a 3-D model with the deeper upper mantle (350 to 800 km) included.
Figure (n) Same as **figure (m)** but for the results of event 2.

Interpretations

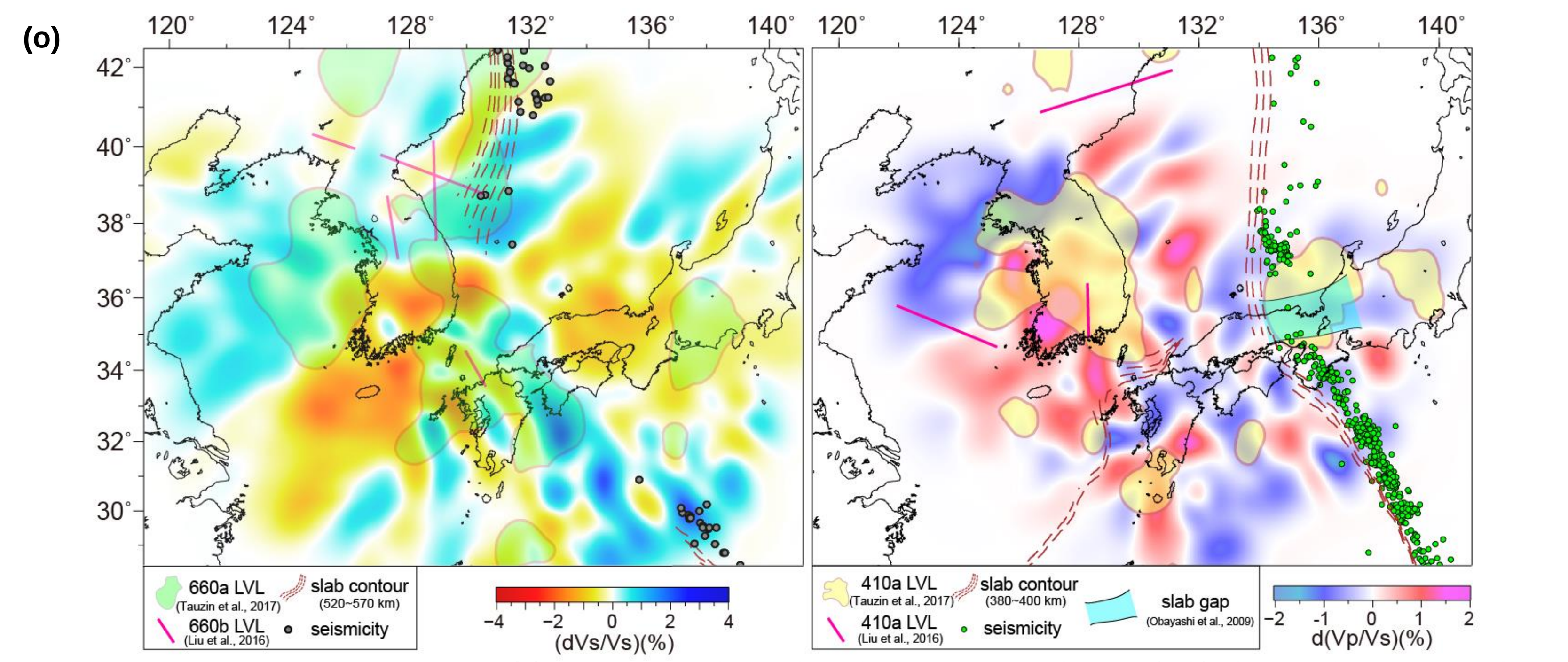

Figure (o) shows tomographic results with main interpreted features. (Left) A horizontal cross-section of Vs at a depth of 535 km. (Right) A horizontal cross-section of the Vp/Vs at a depth of 390 km. Gray dotted lines indicate 410 and 660 km depths. 660a LVL: low-velocity layer above the 660-km discontinuity (Tauzin et al., 2017); 660b LVL: low-velocity layer below the 660-km discontinuity (Liu et al., 2016); 410a LVL: low-velocity layer above the 410-km discontinuity (yellow shaded areas are from Tauzin et al. (2017) and pink profiles are from Liu et al. (2016)). At 660-km depth, we suggest that the observed high-velocity anomalies correspond to slab fragments, and the low-velocity anomalies potentially show slab gap. The high Vp/Vs (~2%) at 390-km depth coincide with a relatively thick (>60 km) 410-km low-velocity layer observed by the receiver function studies, and this anomaly potentially reflects low velocity by the presence of partial melt above 410-km.

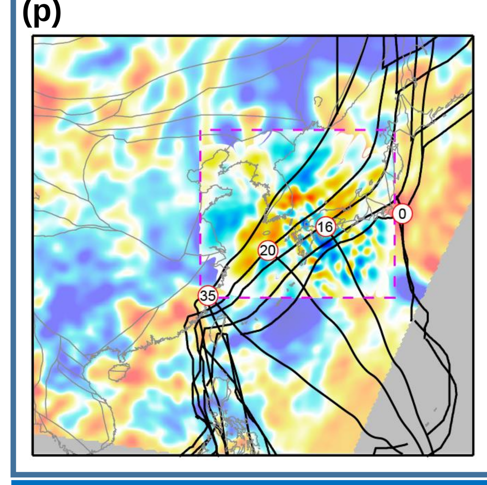

Figure (p) shows comparison of convergent boundaries predicted from plate reconstruction model in northeast Asia margin during the Cenozoic period (35~0 Ma) and the tomography model at 600-km depth. The locations of the plate boundaries are reconstructed from GPlates (Boyden et al., 2011). The velocity models inside and outside of the pink square are from this study and FWEA18 (Tao et al., 2018), respectively. We suggest that the slab gap was formed by tearing of subducting Pacific plate by the migration of the triple junction between the Pacific plate, Philippine Sea plate, and the Eurasian plate along the continental margin.

References

Boyden, J. A., Müller, R. D., Gurnis, M., Torsvik, T. H., Clark, J. A., Turner, M., ... & Cannon, J. S. (2011). Next-generation plate-tectonic reconstructions using GPlates.
Komatitsch, D., & Tromp, J. (1999). Introduction to the spectral element method for three-dimensional seismic wave propagation. Geophysical journal international, 139(3), 806-822.
Laske, G., Masters, G., Ma, Z., Pasyanos, M., 2013, April. Update on CRUST1.0—A 1-degree global model of Earth's crust. In: Geophysical Research Abstract 15, 2658. Vienna, Austria: EGU General Assembly.
Liu, Z., Park, J., & Karato, S. I. (2016). Seismological detection of low-velocity anomalies surrounding the mantle transition zone in Japan subduction zone. Geophysical Research Letters, 43(6), 2480-2487.
Rawlinson, N., Kennett, B. L. N., 2004. Rapid estimation of relative and absolute delay times across a network by adaptive stacking. Geophysical Journal International, 157(1), 332-340.
Rawlinson, N., Sambridge, M., 2004. Wave front evolution in strongly heterogeneous layered media using the fast marching method. Geophysical Journal International, 156(3), 631–647.
Rawlinson, N., Urvoy, M., 2006. Simultaneous inversion of active and passive source datasets for 3-D seismic structure with application to Tasmania. Geophysical Research Letters, 33(24), L24313.
6784-6801.
Tao, K., Grand, S. P., Niu, F., 2018. Seismic structure of the upper mantle beneath Eastern Asia from full waveform seismic tomography. Geochemistry, Geophysics, Geosystems, 19(8), 2732-2763.
Tauzin, B., Kim, S., & Kennett, B. L. N. (2017). Pervasive seismic low-velocity zones within stagnant plates in the mantle transition zone: Thermal or compositional origin?. Earth and Planetary Science Letters, 477, 1-13.

Acknowledgement

This research was funded by the Korea Meteorological Institute (KMI) under Grant KMI2019-00110